Influence of Fluid Convection on Weld Pool Formation in Laser Cladding

A transient 3D transport model was used to generate insight into details of melt pool formation, fluid convection, and solidification in Inconel® 718 laser claddings

BY Y. S. LEE, M. NORDIN, S. S. BABU, AND D. F. FARSON

ABSTRACT

Laser cladding is a relatively fast and precise metal deposition process that has been widely applied to deposit coatings to protect parts from wear and/or corrosion and to rebuild worn surfaces of expensive components such as jet engine turbine blade tips. Economic development of laser cladding process applications is impeded by lack of a capability to accurately predict the results of complex physical phenomena associated with this process. In this paper, a transient 3D transport model was used to generate insight into details of melt pool formation, fluid convection, and solidification in Inconel® 718 laser claddings. The predicted melt pool geometry was validated by comparison to corresponding experimental data. Simulation results showed a notable flat temperature profile in the liquid ahead of the rear melt pool boundary was induced by Marangoni flow. Also, convection patterns associated with the switching of surface tension gradient from positive to negative at a region behind the laser beam focus spot caused the deepest weld pool penetration to be at this location. Temperature gradients (G) and solidification rates (R) in the liquid on the solidification boundary at the back of the melt pool were quantified and solidification mode was predicted by these values. The results illustrated the key role played by fluid convection in the laser cladding process.

KEYWORDS

• Laser • Powder • Deposition • Cladding • Additive Manufacturing
• Inconel® 718 • Weld Pool • Transport Phenomena

Introduction

Laser cladding has been widely used to add protective coatings to metallic surfaces to resist corrosion or wear and to rebuild worn surfaces of structural parts (Ref. 1).These materials can be deposited as powder or wire that is fed directly into the laser-generated melt pool (Ref. 2). In laser cladding with powder, the particles are usually injected into an inert carrier gas that flows through multiple powder feed nozzles spaced annularly around the laser beam as sketched in Fig. 1. The laser beam energy heats and melts some of the particles during flight and others melt when they strike the melt pool surface. The powder particles impinging on the melt pool form the clad deposition layer after solidification.

The development of laser cladding processes for various applications is hindered by the lack of generally applicable accurate models. Development of such models is impeded by the complexities associated with simultaneous injection of powdered metal into the melt pool formed by a focused laser beam. The powder cloud interacts with the laser beam and decreases the laser power density incident on the substrate and a molten pool formed on the substrate. The decrease in laser power due to transmission of the laser beam through the powder cloud is not entirely lost. Some of the lost energy heats powder particles and a portion of this thermal energy is returned to the molten pool by particles that are incident on it. These powder particles also add mass and momentum to the melt pool. These additions affect the fluid temperature distribution and flow patterns and the final shape of the deposited clad layer.

Numerical simulations of the laser cladding process have been developed to add to the understanding of the underlying physical phenomena. Hoadley and Rappaz (Ref. 3) developed a finite element model for laser cladding based on 2D heat conduction coupled with a number of analytical solutions of mass and momentum balances representing deposition of molten clad metal.

Picasso and Rappaz (Ref. 4)

Y. S. LEE and D. F. FARSON (farson.4@osu.edu) *are with Dept. of Materials Science and Engineering, Welding Engineering Program, The Ohio State University, Columbus, Ohio. M. NORDIN is with Rolls Royce Corp., Indianapolis, Ind. S. S. BABU is with Dept. of Mechanical, Aerospace, and Biomedical Engineering, The University of Tennessee, Knoxville, Tenn.*

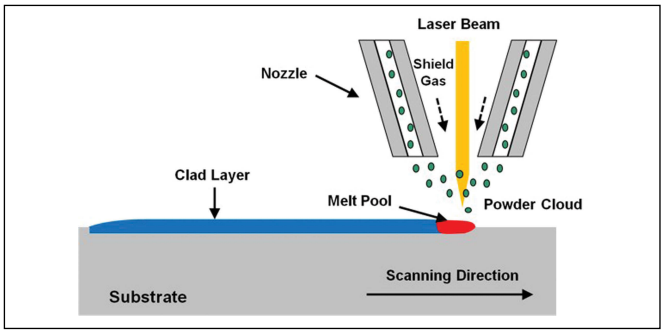

Fig. 1 — Schematic of laser cladding process using coaxial powder feed nozzle

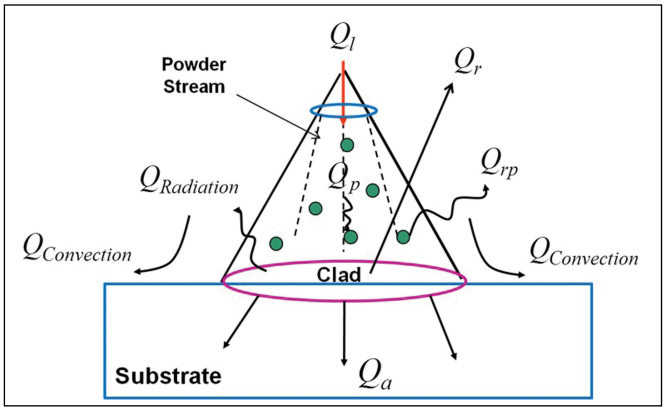

Fig. 3 — Energy balance during laser cladding process.

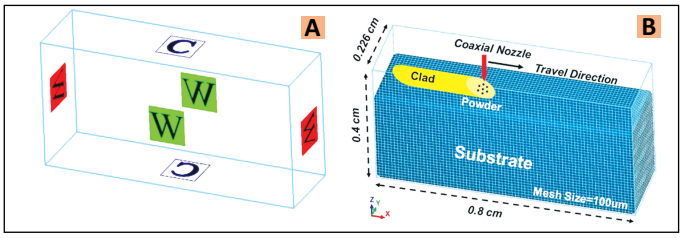

Fig. 2 — A — Boundary conditions for the edges of substrate and powder nozzle; B — description of computation domain.

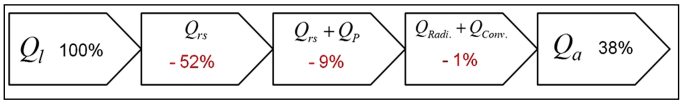

Fig. 4 — Distribution of laser energy in the laser cladding process.

presented two approaches to modeling the laser cladding process in 2D and 3D. The shape of the molten pool was computed at a given laser power in 2D and the laser-powder-material interactions were taken into account in the 3D model.

Toyserkani, Khajepour, and Corbin (Ref. 5) developed a transient finite element model for laser cladding with powder injection in three dimensions. Their model evaluated the correlation of beam velocity and powder feed rate to the clad layer geometry. In this model, the effect of heat flow due to fluid convection was incorporated by modifying the thermal conductivity of the clad layer.

Choi, Han, and Hua (Ref. 6) described a numerical model that included most of the phenomena occurring during the cladding process. A volume of fluid (VOF) simulation method was employed to predict melt pool free surface evolution. They assumed feeding of metal droplets instead of powder particles and constant material properties were used for both liquid and solid metal to simplify the model. The effect of impurities on liquid surface tension was also neglected.

Wen and Shin (Ref. 7) presented a new comprehensive 3D model for the coaxial laser deposition, considering physical phenomena such as laser-powder interaction, fluid motion, mass addition, and solidification. However, they did not account for the effect of surface-active elements on weld pool convection and shape.

Marangoni convection patterns induced by surface-active elements are known to have profound effects on weld pool shape and many previous investigations have been reported with regard to these effects.

Sahoo, DebRoy, and McNallan (Ref. 8) studied the effect of temperature and composition on surface tension of Ni-S system. Lee, Quested, and McLean (Ref. 9) reported temperature-dependent values for the surface tension and its gradient with electron beam melting of two distinct compositions of IN718 (20 ppm S, 8 ppm O, and 6 ppm S, <10 ppm O). Su and Mills (Ref. 10) developed the calculation model for surface tension in IN718 with various sulfur and oxygen concentrations at the ppm level.

Zhao, Kwakernaak, Pan, Richardson, Saldi, Kenjeres, and Kleijn (Ref. 11) reported studies of the effect of oxygen and temperature on surface tension of stainless steels in laser spot welding. However, the effect of surface-active elements and associated convection patterns on the formation of laser melt pools has not been considered in prior laser cladding simulations where mass addition to the melt pool is considered.

The objective of this paper is to describe the formulation of a transient 3D numerical model of the laser cladding process, to compare model predictions of laser clad deposit geometry to experimental measurements and to study the predicted weld pool convection flow patterns. The following sections discuss fundamental physical mechanisms and mathematical models used to represent the laser cladding process, the VOF numerical simulation technique, simulation predictions of single-pass, single-layer clad deposit geometry, and comparisons to experimental measurements and conclusion and issues for further study.

Experimental Conditions

Single clad deposits were produced in autogenous Ni-superalloy IN718 laser cladding. Fiber laser power with uniform intensity (flat-top) of 350 to 550 W was used to build the clad deposit on a 5.08 cm (height) × 5.08 cm (length) × 0.226 cm (thickness) substrate in argon atmosphere. The beam spot diameter and beam travel speed were 1.0 mm and 1.016 cm/s, respectively. Nominal composition of the IN718 powder is shown in Table 1. Metal powder screened with 100–325 mesh was used to build the clad deposit. Samples for metallographic cross sections were mounted, polished, and then etched with standard metallographic method. No preheating or postweld temperature

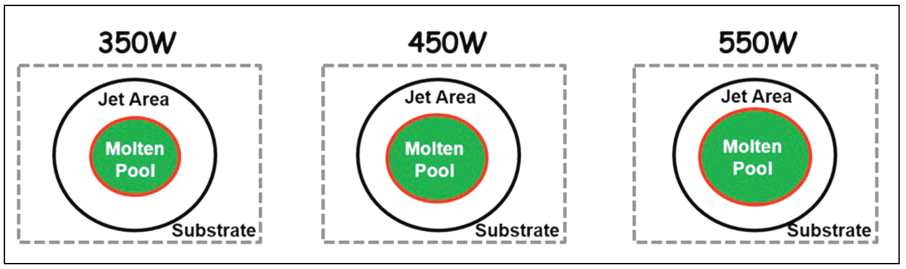

Fig. 5 — Assumption for powder catchment efficiency.

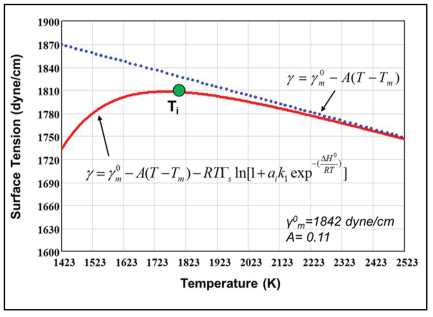

Fig. 6 — The temperature and surface-active element dependent values of surface tension.

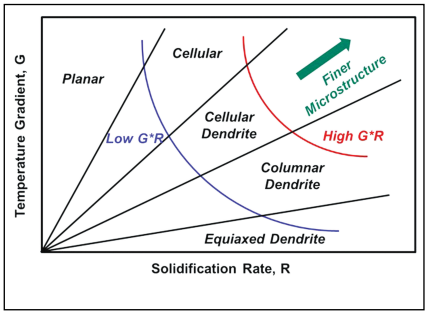

Fig. 7 — Effect of G and R on solidification morphology.

control was used in the experiments. The clad deposit width, height, and penetration were directly measured from optical images using image processing software (ImageJ, NIH) and used to validate the simulation results.

Clad Deposit Modeling

Conservation of mass, energy, and momentum form the basis for expressions used to model the laser cladding melt pool and substrate. Also, it is important to account for the addition of energy by the focused laser beam and the addition of mass, energy, and momentum by the added metal powder for an accurate process model. The VOF method is adopted to simulate the fluid flow in the weld pool and to predict the evolution of weld pool shape, size, and temperature, as well as the temperature distribution in the substrate. In this work, the VOF laser cladding process simulation was implemented by integrating subroutines to represent laser heating and clad powder addition into available transport simulation software (Flow-3D, Flow Science Corp.).

Governing Equations

Three-dimensional mass conservation for VOF simulation of incompressible fluid flow is expressed by the equation

$$\frac{\partial \rho}{\partial t} + \nabla \cdot (\vec{v}\rho) = \dot{m}_s \qquad (1)$$

where ρ is density of fluid in a numerical simulation mesh cell, t is time, $\vec{v}$ is liquid metal velocity, and $\dot{m}_s$ is volumetric mass source rate. This conservation of mass relation can be rewritten in terms of a scalar value F that explicitly refers to the mesh used to discretize the simulation domain. F denotes volume fraction of fluid in a mesh cell defined in the numerical simulation. By definition, the value of F = 0 indicates that the corresponding simulation cell lies entirely within a void region and thus contains no fluid while F = 1 indicates the cell is entirely occupied by fluid. Hence, any cell having F values between 0 and 1 lies on the surface between fluid and void regions. The volume fraction of fluid and volume fraction source rate can be defined in terms of the density of fluid occupying a given cell as Equations 2 and 3

$$\rho = \rho_0 F \qquad (2)$$

$$\dot{m}_s = \rho_0 \dot{F} \qquad (3)$$

where it is reiterated that ρ refers to density of fluid in a cell (ratio of mass of fluid in the cell and cell volume), ρ_0 is density of the fluid, and F is volume fraction of fluid in the cell. A relation for conservation of F can be derived from Equations 1–3, as (Ref. 12)

$$\frac{\partial F}{\partial t} + \nabla \cdot (\vec{v}F) = \dot{F} \qquad (4)$$

By simultaneously solving the time-varying volume fraction conservation law along with the momentum and energy conservation relations presented below, the time-varying location and shape of the fluid-void boundary can be predicted.

For conservation of momentum, the fluid is assumed to be Newtonian with laminar flow (Ref. 13). The resulting conservation equation is

$$\frac{D\vec{v}}{Dt} = -\frac{1}{\rho}\nabla P + \mu\nabla^2\vec{v} + \vec{g} + \frac{\dot{\vec{p}}_s}{\rho} \qquad (5)$$

where P is hydrodynamic pressure, μ is viscosity, $\vec{g}$ is gravitational acceleration, ρ is thermal expansion , and $\dot{\vec{p}}_s$ is a source term representing the momentum addition rate corresponding to the captured filler material droplets.

Table 1 — Nominal Composition of IN718 Powder in wt-%

Element	C	Mn	Si	P	S	Cr	Ni	Mo	Nb	Ta	Ti	Al
Quantity	0.034	0.008	0.09	0.006	<0.0005	18.03	54.62	2.93	5.14	<0.002	0.85	0.59
Element	Co	B	Cu	Pb	Bi	Se	Fe					
Quantity	0.11	0.003	0.11	0.00003	<0.00001	<0.00001	Bal					

Melt pool convection induced by buoyancy force due to thermal expansion of the melt is typically negligible in comparison to flow induced by surface tension gradient and was not included in this simulation.

In the simulations associated with free-surface fluid dynamics, the heat input, in this case from the laser beam, is imposed as part of a surface heat flux boundary condition. The heat is convected and conducted through clad the deposit melt pool and substrate. Conservation of thermal energy used in the simulation is given as

$$\frac{\partial h}{\partial t}+\left(\vec{v}\cdot\nabla\right)h=\frac{1}{\rho}\left(\nabla\cdot\lambda\nabla T\right)+\frac{\dot{h}_s}{\rho} \qquad (6)$$

where h is enthalpy, λ is thermal conductivity, and $\dot{h}_s$ is a source term representing enthalpy addition rate associated with captured filler material droplets. The expression above only considers thermal energy conservation in the weld pool. This is reasonable since weld pools are relatively small and fluid flow speeds are moderate so the kinetic and potential energy of the fluid is much smaller than the thermal energy. The latent heat due to solid to liquid phase change is included in the enthalpy-temperature relationship.

Boundary Conditions and Physical Properties for the Simulation

The boundary conditions applied to the lateral edges of the substrate (illustrated in Fig. 2) were assumed as all solid walls to depict a rigid substrate with convection heat loss coefficient 10^5 erg/cm^2/C. The top and bottom surface boundary conditions were defined as continuous to model semi-infinite domain in the surfaces. Laminar flow and incompressible liquid were assumed for fluid flow in the weld pool. The simulation was modeled in a three-dimensional Cartesian system for description of the transport phenomena. The computation domain has dimensions of 0.8 cm in length (x-direction), 0.226 cm in width (y-direction), and 0.4 cm in height (z-direction) for transient flow shown in Fig. 2. The z-direction has 0.3 cm of substrate and a 0.1-cm void region above the substrate. The domain was meshed with cubic cells with 100 um mesh size. To model laser heating and powder mass, energy and momentum inputs, a moving source of laser energy and mass flux is incorporated into the computation domain just above the top surface of substrate (labeled "Coaxial Nozzle" in Fig. 2B). The initial temperature of the powder particles was assumed to be liquidus temperature. Thus, liquid particles having a diameter of 50 um leave the nozzle exit and are injected into the liquid pool. Mesh size and computation domain size independence of model results was

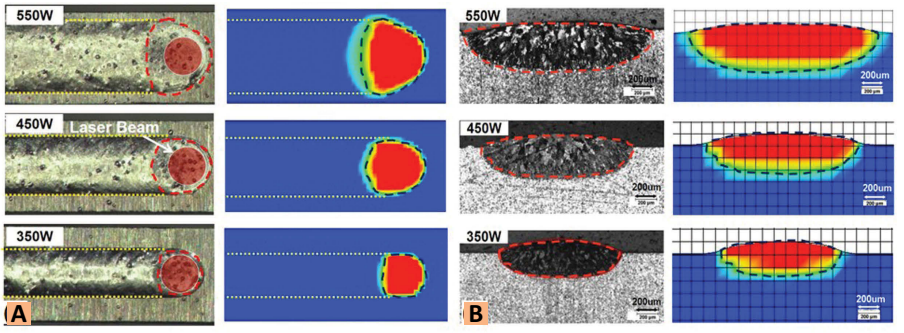

Fig. 8 — A — Top-down; B — cross sectional views at the same magnification for comparison of simulated and experimental single-pass laser clad melt pool and deposits at various powers. Dashed lines in simulation images show the position of liquidus isotherm while dashed lines in experimental images show the liquidus isotherm from the corresponding simulation.

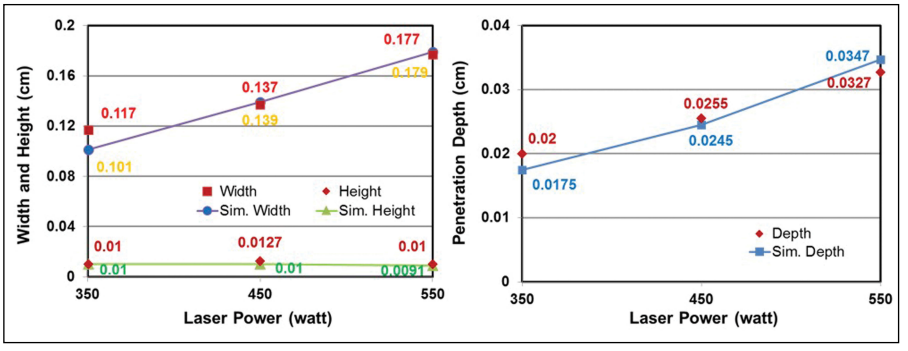

Fig. 9 — Comparison of simulated and experimental weld pool dimensions.

Table 2 — Thermophysical Properties of IN718 and Process Parameters Used in Numerical Model

Property	Symbol	Value	Ref.
Specific Heat of Liquid	C_L	7.25e+06 (cm²/s²/K)	14
Specific Heat of Solid	C_S	5.77e+06 (cm²/s²/K)	14
Conductivity of Liquid	λ_L	2.928e+06 (g-cm/s³/K)	14
Conductivity of Solid	λ_S	2.792e+06 (g-cm/s³/K)	14
Latent Heat	H	2.27e+09 (cm²/s²)	15
Power of Laser Beam	P	350, 450, 550 (W)	—
Beam Spot Size	B_S	1.0 (mm)	—
Powder Feed Rate	—	1.2 (g/min)	—
Powder Particle Size	—	50 (um)	—
Liquidus	T_L	1623 (K)	16
Solidus	T_S	1423 (K)	16
Travel Speed of Laser Beam	V	1.016 (cm/s)	—
Viscosity	η	0.196*exp(5848/T) (MPa)	14
Density of Liquid	D_L	7.3 (g/cm³)	14
Density of Solid	D_S	8.19 (g/cm³)	14

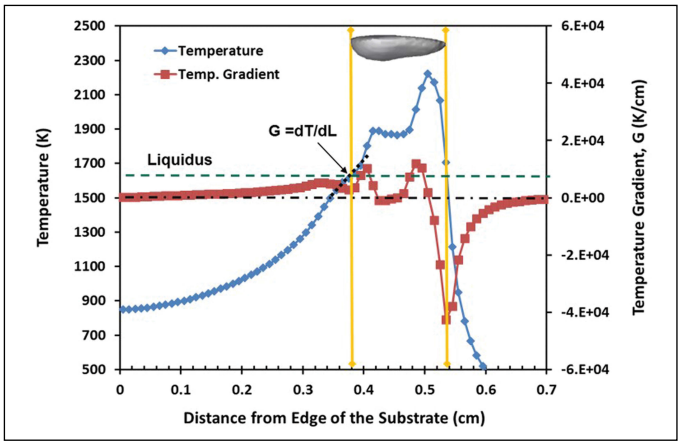

Fig. 10 — Quasi-steady state temperature profile and temperature gradient (G) along the weld pool centerline at time t = 0.43 s.

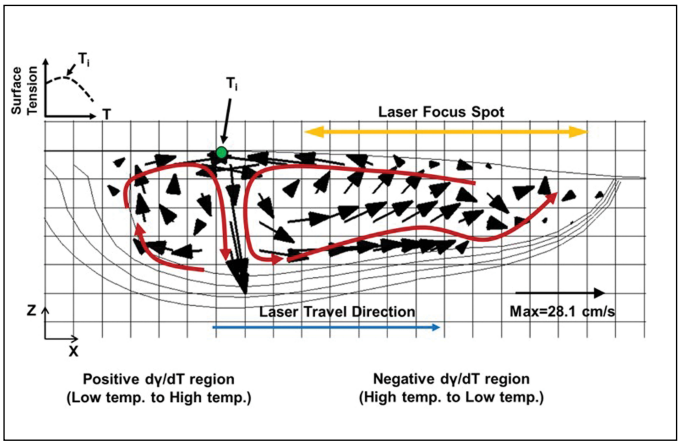

Fig. 11 — Longitudinal-section view showing fluid flow and mixing in the laser clad melt pool, the location of laser focus spot. The green dot indicates the location of the weld pool surface with temperature T_i where surface tension gradient transitions from positive to negative.

verified. The ambient temperature assumed for material and surroundings was 300 K. The material used for both cladding powder and substrate was Ni-based Superalloy IN718. Thermophysical properties and the various welding parameters applied to this simulation are presented in Table 2 (Refs. 14–16). A fiber laser having flat-top distribution was used for this simulation. The laser beam power, beam spot size, powder particle size, and beam travel speed were the values given directly from the cladding process.

Laser Cladding Process Mechanisms and Models

Laser cladding is a fusion welding process that uses a focused, moderate power-density laser beam heat source, and metal powder feed to melt and build up layers of filler material onto a substrate. Modeling of energy conservation in laser cladding needs to account for losses that occur as the laser beam heats the substrate and the powder particles during their flight from the nozzle exit to the substrate, as well as the efficiency of capture of laser powder into the deposited clad layer (Ref. 17). It is important to note that, although laser beam-powder interaction attenuates the laser beam power that is incident on the substrate, not all of the attenuated power is lost since some of it preheats the powder. Most of this portion of this laser power is returned to the cladding process when the heated particles are incorporated into the final clad deposit. Modeling of the laser cladding process should thus take into account absorptance of laser energy by the substrate and by powder particles, substrate and powder melting, transport phenomena in the melt pool, efficiency of capture of powder particles in the clad deposit, and solidification of melt to form a clad deposit. Each of these topics is discussed in more detail in the following.

Absorptance of Laser Beam Energy

Absorptance of laser energy by the clad material is a key laser cladding process parameter that varies with material composition and temperature. It has been found in previous studies that a reasonable estimate of laser energy absorptance is provided by the Hagen-Rubens (Ref. 18) relationship. There, absorptance $A(T)$ of the near-infrared laser energy is calculated from the temperature-varying electrical resistivity of the substrate material $\rho_e(T)$ by the relation

$$A(T) = \left[\delta \varepsilon_0 \omega \rho_e(T)\right]^{1/2} \quad (7)$$

where ω is the angular frequency of the laser radiation (1.75×10^{15} rad/s for fiber laser radiation with wavelength $\lambda = 1.07 \times 10^{-6}$ m) and ε_0 is the permittivity of free space (8.85×10^{-12} F/m). The equation can be rewritten in terms of electrical resistivity as

$$A_{fl}(T) = 354.45\left[\rho_e(T)\right]^{1/2} \quad (8)$$

Expressions for temperature-varying resistivity for solid and liquid IN718 are (Ref. 15)

$$\rho_e(T) = -0.960 + 0.005T - 3.919 \times 10^{-6}T^2 + 9.713 \times 10^{-10}T^3 \quad \text{for solid phase} \quad (9)$$

$$\rho_e(T) = 1.251 + 1.364 \times 10^{-4}T \quad \text{for liquid phase} \quad (10)$$

The calculated optical absorptance at the solidus temperature is 35.6%, which corresponds well to a reported measurement of IN718 absorptance of 36% at T_s (Ref. 19).

Table 3 — Calculation of Catchment Efficiency

Power	Mass Flow Rate Setting (g/s)	Efficiency (%)	Mass Rate into Molten Pool (g/s)
350 W		28.62%	0.00573
450 W	0.020	36.81%	0.00736
550 W		45.00%	0.00900

Energy Balance

In this section, the relations used to calculate the distribution and losses of laser beam power in the laser cladding process are discussed.

Power Balance

The efficiency of use of laser beam power to form a molten clad deposit on a substrate is decreased by power losses due to reflection, radiation, conduction, and convection from both the clad powder and substrate. With reference to the substrate, the power balance can be expressed as (Ref. 17)

$$Q_a = Q_l - Q_{rs} - Q_p - Q_{rp} - Q_{Radi.} - Q_{Conv.} \quad (11)$$

where Q_a is power absorbed by the substrate, Q_l is total power in the laser beam, Q_{rs} is incident laser power reflected by the substrate, Q_p is power absorbed by the fraction of the powder stream that is not included in the clad deposit, Q_{rp} is power reflected from the powder stream, $Q_{Radi.}$ is power lost from the substrate by radiation, and $Q_{Conv.}$ is power lost from the substrate by convection. A visual representation of Equation 11 is shown in Fig. 3. It illustrates how the total laser power is redistributed by powder absorption and the various losses.

Experiment measurements of the power losses noted above have been reported by Gedda (Ref. 17) as 9% for $Q_{rp} + Q_p$, 1% for $Q_{Radi.} + Q_{Conv.}$, and 52% for Q_{rs}. From the values, the fraction of laser power absorbed by the substrate is calculated from Equation 11 as Q_a = 38%. Notice that the reflection from substrate and powder stream are the largest losses from the cladding process. Laser power absorption by an ionized plasma is neglected because the near-infrared laser wavelength (λ = 1.07 m) and moderate focused power density (7×10^4 W/cm^2) yield negligible absorption (Ref. 20). Figure 4 gives schematic flow of energy losses.

Total absorbed energy by the substrate, Q_a can be rewritten as

$$Q_a = Q_c + Q_F \quad (12)$$

where Q_c is the fraction of the total laser power utilized in melting the clad deposit and Q_F is the fraction of total laser power used in heating the substrate. Q_c can be calculated by

$$Q_c = Av\rho(C_p T + H) \quad (13)$$

where A is area of weld bead, v is laser beam travel speed, ρ is density of the melted material, C_p is specific heat of the melted material, T is temperature difference between liquidus and room temperature, and H is latent heat of the clad melt. From the calculation, it is shown that percentages of total laser power used for melting the clad deposit and heating of the substrate are Q_c = 8.4% and Q_F = 29.6%, respectively.

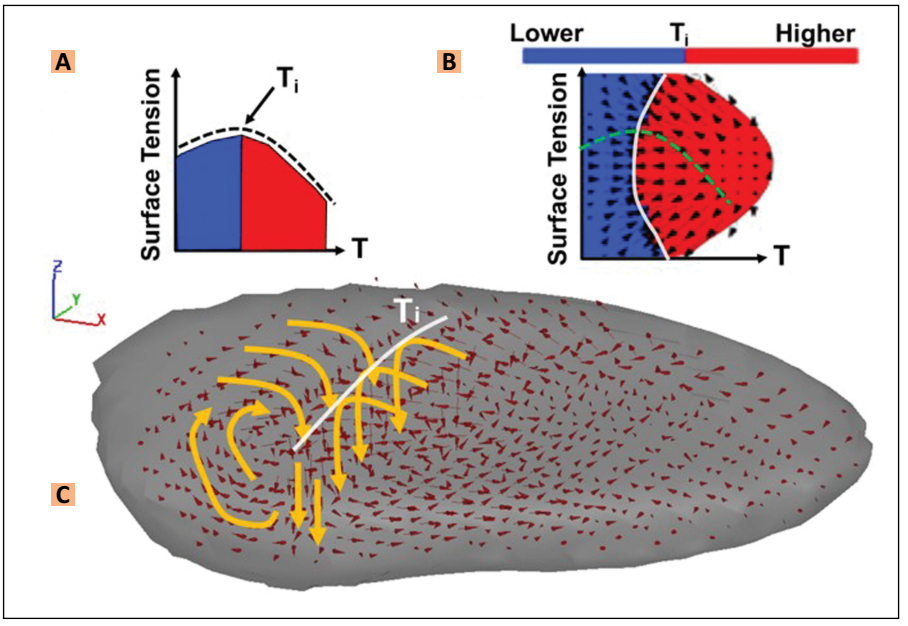

Fig. 12 — Three-dimensional depiction of weld pool convection flows (C) with inset figures showing temperature-dependent surface tension (A) and surface temperature (B). A — Surface tension gradient switches from positive to negative at T_i; B — T_i separates the positive (blue) and negative (red) surface tension regions. The two opposing surface flows impinge along the line where surface temperature equals T_i.

Powder Catchment Efficiency (η)

The powder catchment efficiency can be estimated by the fraction of powder particles that impinge on the molten area of the substrate. For single-pass, single-layer laser cladding, it may be assumed that any particles that strike the melt pool will become part of the clad layer. In this approximation, all particles that do not impinge on the pool can be considered as lost. This is reasonable because powder particles that are not melted during their flight through the laser beam are likely to be reflected from the solid substrate and those that are melted may adhere to the substrate but can still be considered as lost because they do not contribute to formation of the single-pass clad layer. With this assumption and an additional requirement that the powder jet impingement area is larger than the melt pool, powder catchment efficiency can be defined as the ratio between the molten pool area and the substrate area impinged by the power jet (Ref. 21).

$$\eta = \frac{S_{jet}^{liq}}{S_{jet}} \quad (14)$$

Please note that assumptions the molten area can vary with laser power change and jet area is larger than the molten pool area in this computation, which are depicted in Fig. 5. Jet area is constant for different laser powers while the molten pool area increases proportionally as a function of the laser power.

Melt Pool Fluid Surface Tension

The variation of surface temperature across the laser melt pool surface caused fluid surface tension gradients

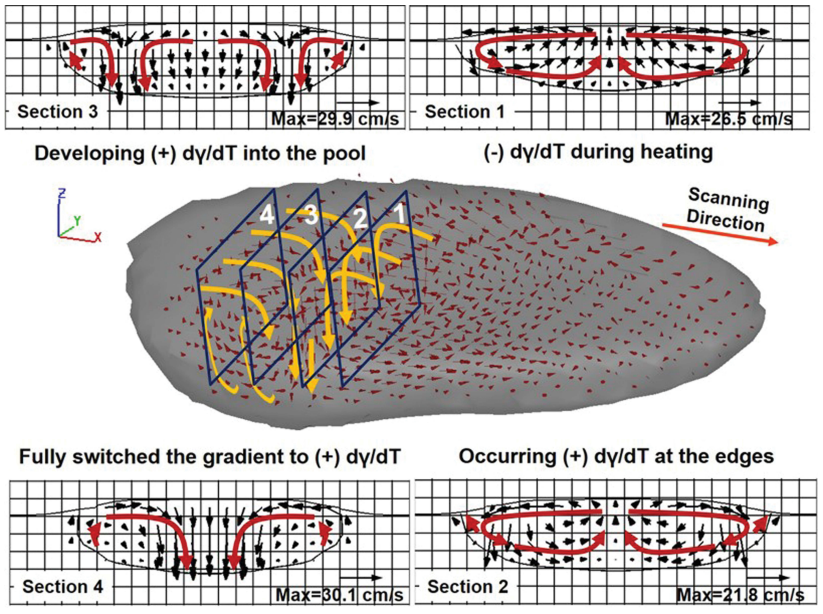

Fig. 13 — 3D and 2D plots showing fluid flow and mixing in the laser clad melt pool.

and induced surface fluid flow from low to high surface tension regions. Such Marangoni flows have been found to have significant effects on weld pool circulation patterns and weld pool shape (Ref. 22). The amount of surface-active element sulfur in the alloy strongly affects the sign and magnitude of surface tension gradients and associated Marangoni flow. It has been reported that the behavior of sulfur in IN718 can be assumed to be the same as that in Fe-Ni-Cr alloys (Ref. 9). Thus, in this study, the behavior of sulfur is accounted for by an equation applicable to an Fe-Ni-Cr-S alloy (Ref. 23). Also, the effect of Cr-S interaction is considered in an activity term since Cr changes the activity of S whereas Ni has negligible effects on the activity of S. The values of surface tension gradient used in the simulation were calculated using Equation 15 and material properties (Refs. 14, 23–25).

$$\gamma = \gamma_m^o - A\left(T - T^0\right) - R\Gamma_s \ln\left[1 + a_i k \exp\left(-\left(\frac{\Delta H^o}{RT}\right)\right)\right] \quad (15)$$

Here γ^0_m = 1842 dyne/cm is the surface tension of the pure metal at reference melting temperature T^0, A = 0.11 is a coefficient for the variation of surface tension at temperature T above the liquidus, R = 8.314 J/mol-K is the gas constant, Γ_s = 2.27 $\times 10^{-9}$ g-mol/cm^2 is surface excess at saturation, $k = 3.18 \times 10^{-3}$ is entropy segregation constant, and $\Delta H^0 = -1.661 \times 10^{-5}$ J/mol is enthalpy of segregation. a_i is the activity of species i in solution. For the alloy used in the present study, transition temperature of surface tension gradient is predicted at 1801 K, marked as T_i in Fig. 6.

Melt Solidification

In metal alloys, it is known that solidification morphology is significantly affected by the combination of temperature gradient (G) in the liquid at the solidification boundary and solidification rate (R) as presented in Fig. 7 (Ref. 26).

A planar growth mode occurs when G is very high or/and R is extremely low value. As R increases, the solidification morphology can shift to cellular, columnar, and then equiaxed dendritic. Most metal alloys solidify in cellular or columnar dendritic mode. The cellular and columnar growth modes are produced when the growth of crystal structures occurs without formation of any secondary dendrite arms. If additional dendrite arms form, the solidification mode shifts to dendritic. Equiaxed dendritic morphology is possible only when G is very low.

As the cooling rate, which is the product of G and R, increases, finer microstructures are produced. Note that high cooling rate results in much closer spacing between cellular or dendrite arms. Eventually, the finer microstructure leads to increased mechanical properties. In general, it is known that cooling rate in laser cladding varies with the processing parameters (Ref. 2) and is faster (10^2 –10^6 K/s) than that of conventional casting. Therefore, the influence of processing parameters on G and R and the solidification morphologies that occur will be assessed in this study.

Results and Discussion

Powder Catchment Efficiency

The metal powder catchment efficiency (Ref. 27) and resulting mass flow rate of powder into the melt pool used in the simulation were calculated from experimental results and results given in the literature. As shown in Table 3, the catchment efficiency was 45% and the mass flow rate was 1.2 g/min for a 550-W laser. The mass flow rates at 350 and 450 W were proportionally adjusted from the 550-W value based on the laser power ratio. Lower laser power creates a smaller molten area on the substrate, S^{liq}_{jet} according to Equation 14. By scaling, the molten pool area at 350 W is 63.6% of the area at 550 W. From the assumptions, the efficiencies for 350 and 450 W are calculated to be 28.62 and 36.81%, respectively.

Melt Pool Size: Experiment vs. Simulation

The width, height, and penetration depth of the deposit are compared to the simulation results by X-Y (A) and Y-Z (B) views in Fig. 8A, B. A dotted line indicating the simulation liquid-solid weld pool boundary is overlaid onto each corresponding experimental image. These results show that simulated weld pool shapes and dimensions are comparable to the experiments. Quantitative comparisons of

simulated and experimental clad width, height, and penetration depth are shown in Fig. 9. The weld pool dimensions are plotted for laser powers of 350, 450, and 550 W. The experimental results are comparable to the simulation predictions. Note that increased laser power leads to increased weld width and penetration depth while the clad height is relatively constant. The clad height is relatively constant because the powder flux within the jet area is constant and the jet area is larger than the weld pool surface area in all simulation cases (cf. Fig. 5). Thus, the larger melt pool surface area results in increased powder catchment efficiency and more mass addition to the molten pool (cf. Table 3), but not increased clad height.

Fluid Flow Patterns in Melt Pool

As discussed in the section titled Melt Pool Fluid Surface Tension, a fluid circulation known as Marangoni flow occurs on the weld pool surface. Resulting convective flow in the melt produces weld pool temperature gradients. Figure 10 shows the temperature profile and corresponding temperature gradient, G, along the clad centerline t = 0.43 s. The quasi-steady state solidification rate on the weld centerline at the back of the weld pool is constant and equal to the laser travel speed, 1.016 cm/s. The calculated values of G = $3.0*10^3$ K/cm and R = 1.016 cm/s are comparable to values found in literature (Ref. 28) for the observed columnar dendritic solidification mode. Although other conditions in the above cited reference vary somewhat from those applicable for laser cladding, it is reasonable to expect similar solidification morphology. The simulated weld pool shape is shown in a gray inset to explain the relationships between temperature profiles, temperature gradient, fluid flow pattern, and weld pool shape. The orange line indicates the weld pool length, which ranges from 0.380 to 0.537 cm at the simulation time 0.43 s. Surface temperature on the weld centerline increases from liquidus at the back of the pool to about 1900 K and then remains constant over a region that also corresponds to the deepest weld pool penetration. Further toward the front of the pool, the surface is heated by laser beam heat input, and the temperature increases further. The variation of weld pool centerline surface temperature gradient is calculated as the first derivative of surface temperature. The temperature gradient equals zero near the center of the laser focus spot (around 0.5 cm) and becomes negative at the front edge of the pool. Note that the deep-penetration region of the weld pool has a flat centerline surface temperature profile and relatively small temperature gradient. It can be reasoned that the flat profile can be attributed to convective fluid flow patterns in the regions toward the back of the weld pool.

Figure 11 displays the flow pattern in the weld pool. Surface areas with positive and negative surface tension gradient are both found on this weld pool. The transition temperature T_i that divides the two regions is calculated from Equation 15 and displayed in the plot in Fig. 6. Its location on the pool surface is represented with a green dot in Fig. 11. Surface tension gradients generate surface flow from areas with low surface tension to areas with high surface tension. Thus, surface flow tends to carry higher temperature fluid from the area heated by the laser beam toward the trailing edge. However, at the same time, flows originating at the cooler back edge of the pool tend to deliver lower temperature fluid toward the front. The two opposing surface flows end up colliding and mixing in a region intermediate between the laser focus spot and the trailing pool edge where the liquid surface temperature is equal to the transition temperature T_i (represented by the green dot in Fig. 11). As a result of the mixing of opposing hotter and cooler flows from the front and rear portions of the melt pool, temperature is relatively uniform in that region and gradient is correspondingly small (cf. Fig. 10). Also, the downward flow (produced by colliding surface flows) is strongest and the resulting weld pool penetration is deepest near this point. Although experimental validation of this weld pool penetration contour has not been completed, the fact that simulation predictions of clad penetration, width, and height are close to experimental values provides indirect evidence that the weld pool contour is reasonable. We also note that a similar pool profile has been predicted in autogenous gas tungsten arc welding (Ref. 29).

The weld pool surface tension and fluid flow patterns are shown in 2D and 3D plots in Fig. 12. It is seen that two opposing flows meet at the line showing the position of the transition temperature T_i (Fig. 12B) and generate downward mixing flow along this line (Fig. 12C). In Fig. 13, the variation of fluid flow patterns are assessed in consecutive 2D cross sections spaced evenly along the X-axis.

Dominant outward-directed Y-axis Marangoni flows are observed on the weld surface with maximum velocity 26.5 cm/s in section 1. This pattern of the flow indicates only negative surface tension gradient resulting in completely outward flow is present at this region. In section 2, the main Marangoni flow is still outward direction at the center of the weld pool due to negative surface tension gradient and relatively high temperature at that region. Note that inward fluid flows that are opposite to the flow at the center in direction are observed near the outermost edges of the pool. This flow pattern indicates switching of surface tension gradient from negative to positive. The fluid velocity is reduced to 21.8 cm/s due to the opposing flow. In section 3, prominent inward and outward surface flows with comparable velocities exist. Downward flow is found at the intermediate region between the weld edge and center where the surface flows collide. As the distance from the laser beam increases, weld pool temperature decreases, and eventually it reaches the temperature switching surface tension gradient. Hence, the region showing the dominant positive gradient keeps widening but the expansion stops at the gradient transition region. The maximum flow velocity is found at the region where the two opposite flows meet. In section 4, the gradient is fully switched to positive. Thus, only inward and downward flows are seen.

Summary, Conclusions, and Future Work

A transport simulation of the laser

cladding process was used to understand the effect of convection flow on the cladding melt pool formation and solidification conditions in IN718 deposits. Predicted clad width, height, and penetration depth at different laser powers were found to be comparable to experimental measurements. Due to heat flow in the melt pool induced by Marangoni convection, the most deeply penetrated region was formed toward the back of the weld pool, behind the laser focus spot but ahead of the rear solidification boundary. The increased penetration was formed in this region by impingement of opposing surface flows caused by positive and negative X-axis surface tension gradients along the weld centerline. The flow pattern also caused the weld pool to have a relatively flat rear boundary and contributed to a relatively uniform temperature distribution in the melt pool in the region where opposing surface flows impinged. Also, temperature gradient was calculated along the weld pool centerline and, in combination with the centerline solidification rate at the back edge of the weld pool, was used to predict columnar dendritic solidification. The correspondence with the observed weld pool solidification mode was noted. Future simulation and experimental efforts are planned to extend the work to multiple-layer clads and to experimentally validate the weld pool convection patterns and penetration profiles predicted by the simulations.

References

1. Zhong, M., and Liu, W. 2010. Laser surface cladding: The state of the art and challenges. *Journal of Mechanical Engineering Science* 224(C5): 1041–1060.

2. Weisheit, A., Gasser, A., Backes, G., Jambor, T., Pirch, N., and Wissenbach, K. 2013. *Laser-Assisted Fabrication of Materials — Direct Laser Cladding, Current Status and Future Scope of Application*. pp. 221–240, New York, N.Y.: Springer.

3. Hoadley, A. F. A., and Rappaz, M. 1992. A thermal model of laser cladding by powder injection. *Metallurgical Transactions B* 23(5): 631–642.

4. Picasso, M., and Rappaz, M. 1994. Laser-powder-material interactions in the laser cladding process. *Journal De Physique IV* 4(C4): 27–33.

5. Toyserkani, E., Khajepour, A., and Corbin, S. 2004. 3-D finite element modeling of laser cladding by powder injection: Effects of laser pulse shaping on the process. *Optics and Lasers in Engineering* 41(6): 849–867.

6. Choi, J., Han, L., and Hua, Y. 2005. Modeling and experiments of laser cladding with droplet injection. *Journal of Heat Transfer* 127(9): 978–986.

7. Wen, S., and Shin, Y. C. 2010. Modeling of transport phenomena during the coaxial laser direct deposition process. *Journal of Applied Physics* 108(4): 044908.

8. Sahoo, P., DebRoy, T., and McNallan, M. J. 1988. Surface tension of binary metal-surface active solute systems under conditions relevant to welding metallurgy. *Metallurgical Transactions B* 19B(3): 483–491.

9. Lee, P. D., Quested, P. N., and McLean, M. 1998. Modelling of Marangoni effects in electron beam melting. *Philosophical Transactions of the Royal Society of London* 356(1739): 1027–1043.

10. Su, Y., and Mills, K. C. 2005. A model to calculate surface tension of commercial alloys. *Journal of Materials Science* 40(9-10): 2185–2190.

11. Zhao, C. X., Kwakernaak, C., Pan, Y., Richardson, I. M., Saldi, Z., Kenjeres, S., and Kleijn, C. R. 2010. The effect of oxygen on transitional Marangoni flow in laser spot welding. *Acta Materialia* 58(19): 6345–6357.

12. Cho, M. H., Lim, Y. C., and Farson, D. F. 2006. Simulation of weld pool dynamics in the stationary pulsed gas metal arc welding process and final weld shape. *Welding Journal* 85(12): 271-s to 283-s.

13. Cho, J. H., Farson, D. F., Milewski, J. O., and Hollis, K. J. 2009. Weld pool flows during initial stages of keyhole formation in laser welding. *Journal of Physics D: Applied Physics* 42(17): 175502.

14. Mills, K. C. 2002. Recommended values of thermophysical properties for selected commercial alloys. pp. 181–190, Cambridge, England: Woodhead.

15. Pottlacher, G., Hosaeus, H., Kaschnitz, E., and Seifter, A. 2002. Thermophysical properties of solid and liquid Inconel 718 alloy. *Scandinavian Journal of Metallurgy* 31(3): 161–168.

16. Lewandowski, M. S., and Overfelt, R. A. 1999. High temperature deformation behavior of solid and semi-solid alloy 718. *Acta Materialia* 47(18): 4695–4710.

17. Gedda, H., Powell, J., Wahlstrom, G., Li, W. B., Engstrom, H., and Magnusson, C. 2002. Energy redistribution during CO_2 laser cladding. *Journal of Laser Applications* 14(2): 78–82.

18. Xie, J., Kart, A., Rothenflue, J. A., and Latham, W. P. 1997. Temperature-dependent absorptivity and cutting capability of CO_2, Nd:YAG and chemical oxygen-iodine lasers. *Journal of Laser Applications* 9(2): 77–85.

19. Shelton, J. A., and Shin, Y. C. 2010. Comparative evaluation of laser-assisted micro-milling for AISI 316, AISI 422, TI-6Al-4V and Inconel 718 in a side-cutting configuration. *Journal of Micromechanics and Microengineering* 20(7): 075012.

20. Kim, K. R., and Farson, D. F. 2001. CO_2 laser-plume interaction in materials processing. *Journal of Applied Physics* 89(1): 681–688.

21. Picasso, M., Marsden, C. F., Wagniere, J. D., Frenk, A., and Rappaz, M. 1994. A simple but realistic model for laser cladding. *Metallurgical and Materials Transactions B* 25B(2): 281–291.

22. Kou, S. 2012. Fluid flow and solidification in welding: Three decades of fundamental research at the University of Wisconsin. *Welding Journal* 91(11): 287-s to 302-s.

23. Zacharia, T., David, S. A., Vitek, J. M., and DebRoy, T. 1989. Weld pool development during GTA and laser beam welding of type 304 stainless steel — Part I: Theoretical analysis. *Welding Journal* 68(12): 499-s to 509-s.

24. McNallan, M. J., and DebRoy, T. 1991. Effect of temperature and composition on surface tension in Fe-Ni-Cr alloys containing sulfur. *Metallurgical Transactions B* 22B(4): 557–560.

25. Anderson, T. D., Dupont, J. N., and DebRoy, T. 2010. Origin of stray grain formation in single-crystal superalloy weld pools from heat transfer and fluid flow modeling. *Acta Materialia*. 58(4): 1441–1454.

26. Kou, S. 2003. *Welding Metallurgy*. P. 166, New Jersey: John Wiley & Sons.

27. Weisheit, A., Backes, G., Stromeyer, R., Gasser, A., Wissenbach, K., and Poprawe, R. 2001. Powder injection: the key to reconditioning and generating components using laser cladding. *Proceedings of International Congress on Advanced Materials, Their Processes and Applications*, Materials Week 2001, Munich, Germany, pp. 1–7.

28. Lim, Y. C., Yu, X., Cho, J. H., Sosa, J., Farson, D. F., Babu, S. S., McCracken, S., and Flesner, B. 2010. Effect of magnetic stirring on grain structure refinement — Part I: Autogenous nickel alloy welds. *Science and Technology of Welding and Joining* 15(7): 583–589.

29. Zhao, Y. Z., Lei, Y. P., and Shi, Y. W. 2005. Effects of surface-active elements sulfur on flow patterns of welding pool. *Journal of Materials Science and Technology* 21(3): 408–414.